ADVANCED ENERGY MATERIALS
www.advenergymat.de

Impurities in Na_2S Precursor and Their Effect on the Synthesis of W-Substituted Na_3PS_4: Enabling 20 mS cm^{-1} Thiophosphate Electrolytes for Sodium Solid-State Batteries

*Felix Schnaubelt, Arpita Panda, Daniel Wagner, Maya Ziegler, Hoang A. Dang, Wolfgang G. Zeier, Anja Bielefeld, and Jürgen Janek**

Sodium solid-state batteries are intensively researched, expecting a resource-uncritical alternative to their lithium counterparts. As in the case of lithium, sulfide-type electrolytes show promising ionic conductivities σ, and Na_3PS_4-type solid electrolytes are intensively investigated. Aliovalent substitution of P^{5+} by W^{6+} is shown to achieve sodium ion conductivity $\sigma(Na^+)$ beyond 10 mS cm^{-1}, rendering them good candidates for cathode composites. Yet, incorporating WS_4^{2-} into the crystal lattice of Na_3PS_4 is deemed challenging, and $Na_{3-x}P_{1-x}W_xS_4$ electrolytes suffer from WS_2 residue after synthesis. In this work, impurities in the precursor Na_2S are identified and the detrimental influence of SO_x groups in Na_2S on the synthesis of Na_3PS_4 and $Na_{3-x}P_{1-x}W_xS_4$ is demonstrated. The behavior of oxygen as impurity during synthesis is pinpointed, and complete incorporation of tungsten up to $x \approx 0.25$ in $Na_{3-x}P_{1-x}W_xS_4$ by purified Na_2S, realizing up to $\sigma(Na^+) = 26.4$ mS cm^{-1} at room temperature.

1. Introduction

Inorganic solid electrolytes are a key component of solid-state battery cells, which are developed as potential high-energy and power density storage devices.[1] To achieve the desired combination of high energy and power density, highly conducting solid electrolytes are needed, particularly as electrode components.[2] Modeling studies show that solid electrolytes with $\sigma_{ion} > 10$ mS cm^{-1} are required to enable thick cathode composites with high rate capability.[3] Despite extensive scientific work during the last decade, only few lithium-based solid electrolytes, mainly highly substituted argyrodites and $Li_{10}GeP_2S_{12}$-type electrolytes, achieve such high $\sigma(Li^+)$ at 25 °C.[4–6] $Li_{9.54}[Si_{0.6}Ge_{0.4}]_{1.74}P_{1.44}S_{11.1}Br_{0.3}O_{0.6}$ ($Li_{10}GeP_2S_{12}$-type) reaches the highest $\sigma(Li^+) = 32$ mS cm^{-1} of that electrolyte class at 25 °C up to this date.[7] Recently, also niobium- and tantalum-based lithium oxyhalides are reported to achieve $\sigma(Li^+) > 10$ mS cm^{-1} at room temperature.[8,9]

Sodium-based solid-state cell concepts picked up growing research interest because they require only readily available and resource-uncritical materials.[10] Sulfide-based solid electrolytes like $Na_{11}Sn_2PS_{12}$,[11,12] Na_3PS_4,[13,14] and Na_3SbS_4[15] have been reported to achieve $\sigma(Na^+)$ up to the low 1 mS cm^{-1} range but fail yet to approach $\sigma(Na^+) = 10$ mS cm^{-1}. Pure Na_3PS_4 and Na_3SbS_4 suffer from a lack of unoccupied Na^+ sites, which hinders fast ion mobility.[16,17] To further increase $\sigma(Na^+)$, substitution of S^{2-} with Cl^-,[16,18] or Se^{2-},[19] and Na^+ with Ca^{2+} is reported[20] but only the aliovalent substitution of the central ion in the MS_4^{3-} tetrahedra (M = P^{5+}/Sb^{5+}) with W^{6+} has so far enabled $\sigma(Na^+) > 10$ mS cm^{-1} at 25 °C reproducibly.[17,21–23] The highest reported reliable data for $\sigma(Na^+)$ of the $Na_{3-x}P_{1-x}W_xS_4$ compound is $\sigma(Na^+) = 13$ mS cm^{-1} and $\sigma(Na^+)$ in the 30–40 mS cm^{-1} range for $Na_{3-x}Sb_{1-x}W_xS_4$.[17,21]

The high $\sigma(Na^+)$ in Na_3PS_4-type electrolytes is often partially attributed to the stabilization of the high-temperature cubic polymorph at room temperature.[14,17,21] Recently, it was shown by measurements of the pair distribution function (PDF) that the apparent cubic global structure of Na_3PS_4 and $Na_{2.9}Sb_{0.9}W_{0.1}S_4$ has local tetragonal ordering at room temperature and that the unknown concentration of sodium vacancies V_{Na^+} might be the main reason for the increased $\sigma(Na^+)$ of these materials.[23,24] However, the influence of precursor quality on the synthesis and

F. Schnaubelt, D. Wagner, M. Ziegler, H. A. Dang, A. Bielefeld, J. Janek
Institute of Physical Chemistry and Center for Materials Research
Justus Liebig University Giessen
Heinrich-Buff-Ring 17, 35392 Giessen, Germany
E-mail: juergen.janek@uni-giessen.de
A. Panda, W. G. Zeier
Institute of Inorganic and Analytical Chemistry
University of Münster
48149 Münster, Germany
W. G. Zeier
Institute of Energy Materials and Devices (IMD)
IMD-4: Helmholtz-Institut Münster
Forschungszentrum Jülich
48149 Münster, Germany

The ORCID identification number(s) for the author(s) of this article can be found under https://doi.org/10.1002/aenm.202503047

DOI: 10.1002/aenm.202503047

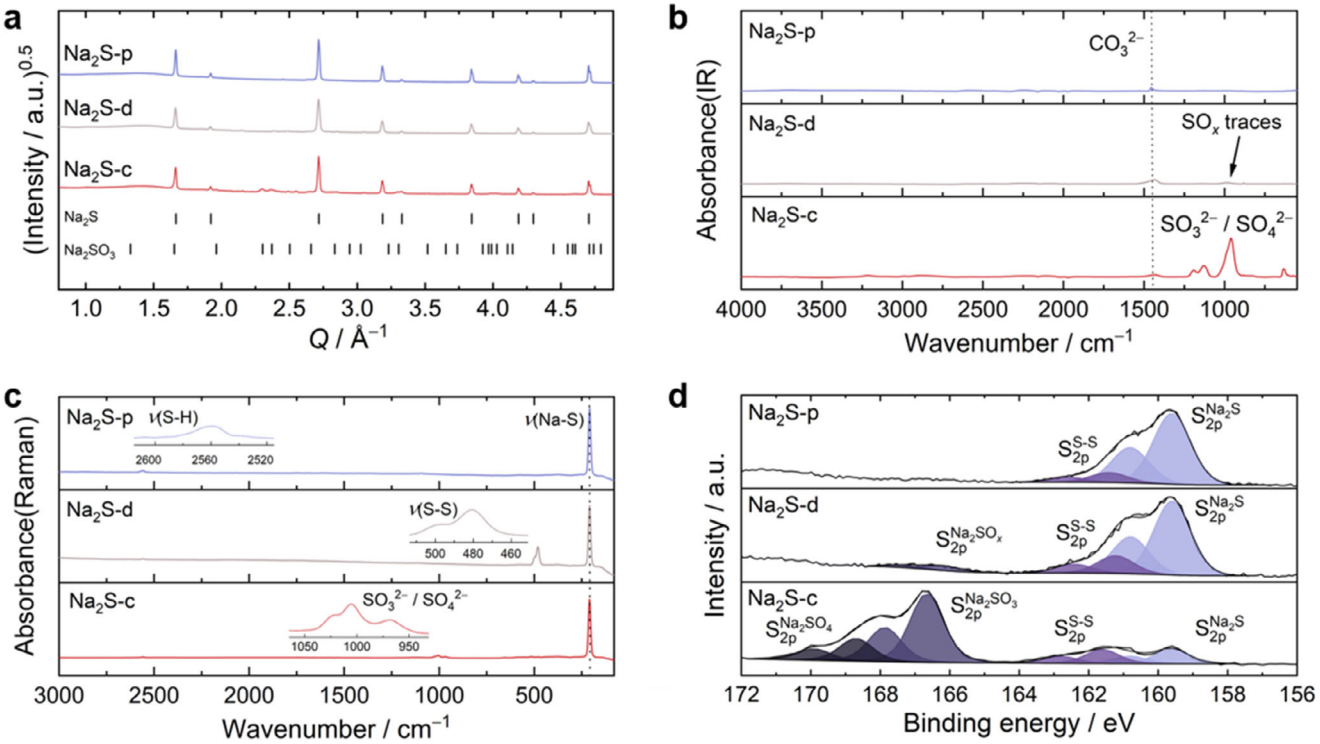

Figure 1. a) Diffraction patterns, b) IR spectra, c) Raman spectra, and d) XP spectra of Na_2S-p, Na_2S-d, and Na_2S-c, respectively. Na_2S-c suffers from SO_x groups, while Na_2S-d contains mostly Na_2S_x contamination. Bragg positions of cubic Na_2S and anhydrous Na_2SO_3 are indicated. A Rietveld refinement of Na_2S-c can be found in the Supporting Information (S4).

resulting $\sigma(Na^+)$ of those electrolytes, i.e., the role of purity in general, is not well understood. In fact, impurities are often used as an explanation for discrepancies between simulated and measured $\sigma(Na^+)$.[22] Yet, even in the case of virtually pure Na_3PS_4, contradicting results are reported. Hayashi et al. found a significant influence of Na_2S purity on $\sigma(Na^+)$, while Nguyen et al. reported no significant effect when conducting Na_3PS_4 synthesis with different Na_2S samples.[13,25] For Na_3SbS_4, an increased $\sigma(Na^+)$ was reported when self-synthesized Na_2S was used, supporting the results of Hayashi et al.[26]

This work aims to resolve these apparent discrepancies and to deepen the understanding of the influence of synthesis conditions on the resulting solid electrolytes and their $\sigma(Na^+)$. As a result, we demonstrate the critical role of Na_2SO_x in Na_2S on $\sigma(Na^+)$ of Na_3PS_4 and the often-overlooked $Na_{3-x}P_{1-x}W_xS_4$ substitution variant. Using optimized and reproducible synthesis conditions, aliovalent substitution of P^{5+} by W^{6+} up to $x \approx 0.25$ is achieved. This leads to the highest $\sigma(Na^+)$ for $Na_{3-x}P_{1-x}W_xS_4$ reported to date – with $\sigma(Na^+) = 15.5$ mS cm^{-1} (cold-pressed powder) and $\sigma(Na^+) = 26.4$ mS cm^{-1} (sintered pellet) for $Na_{2.8}P_{0.8}W_{0.2}S_4$ at 25 °C.

2. Results and Discussion

2.1. Na_2S Purification and Identification of Impurities

To investigate the influence of impurities in Na_2S on the synthesis of $Na_{3-x}P_{1-x}W_xS_4$ electrolytes, technical grade Na_2S was either dried (Na_2S-d) or dried and additionally purified (Na_2S-p). The purification was conducted according to a modified procedure from Smith et al. through heating of Na_2S under a hydrogen atmosphere,[27] and Na_2S-d and Na_2S-p are compared to commercial anhydrous Na_2S (Na_2S-c). The structure of cubic Na_2S was verified by XRD measurements (**Figure 1a**) for all samples.[28] Only Na_2S-c shows additional reflections corresponding to anhydrous Na_2SO_3.[29] In Na_2S-c and Na_2S-d, minor unidentified reflections are observed, which could be caused by hydrate residues (S4). Results from IR measurements (Figure 1b), which are more sensitive for SO_x groups, reveal IR bands between $\nu = [600, 1200]$ cm^{-1} in Na_2S-c, typical for Na_2SO_3 and Na_2SO_4.[30,31] Only a trace amount of SO_x groups is observed in Na_2S-d, which are not observed after purification (Na_2S-p). All samples show low fractions of Na_2CO_3, indicated by weak IR bands at $\nu = 1430$ cm^{-1}.[32] Raman measurements (Figure 1c) were conducted to detect polysulfides, which are found in Na_2S-d at $\nu = \{481, 498\}$ cm^{-1}.[27,33,34] For Na_2S-c, contaminations are detected at $\nu = \{967, 1005, 1025\}$ cm^{-1} which fall in the typical range of Na_2SO_3 and Na_2SO_4.[32,35–38] For Na_2S-p, a weak Raman band at $\nu = 2560$ cm^{-1} indicates NaSH, which could stem from reduced polysulfides during purification.[39] All samples show a strong vibrational mode of Na_2S at $\nu = 207$ cm^{-1}.[27,40,41] XP S2p spectra (Figure 1d) further support the IR results. For Na_2S-c, two SO_x-related peaks at a binding energy (BE) of BE = {166.9, 168.9} eV are observed, which can be attributed to Na_2SO_3 and Na_2SO_4, respectively.[42,43] The very intense peaks contrast with the diffraction pattern of Na_2S-c, which shows Na_2S as the main phase. This indicates inhomogeneous distribution of Na_2SO_x in Na_2S and its accumulation at the powder surface. All spectra show Na_2S

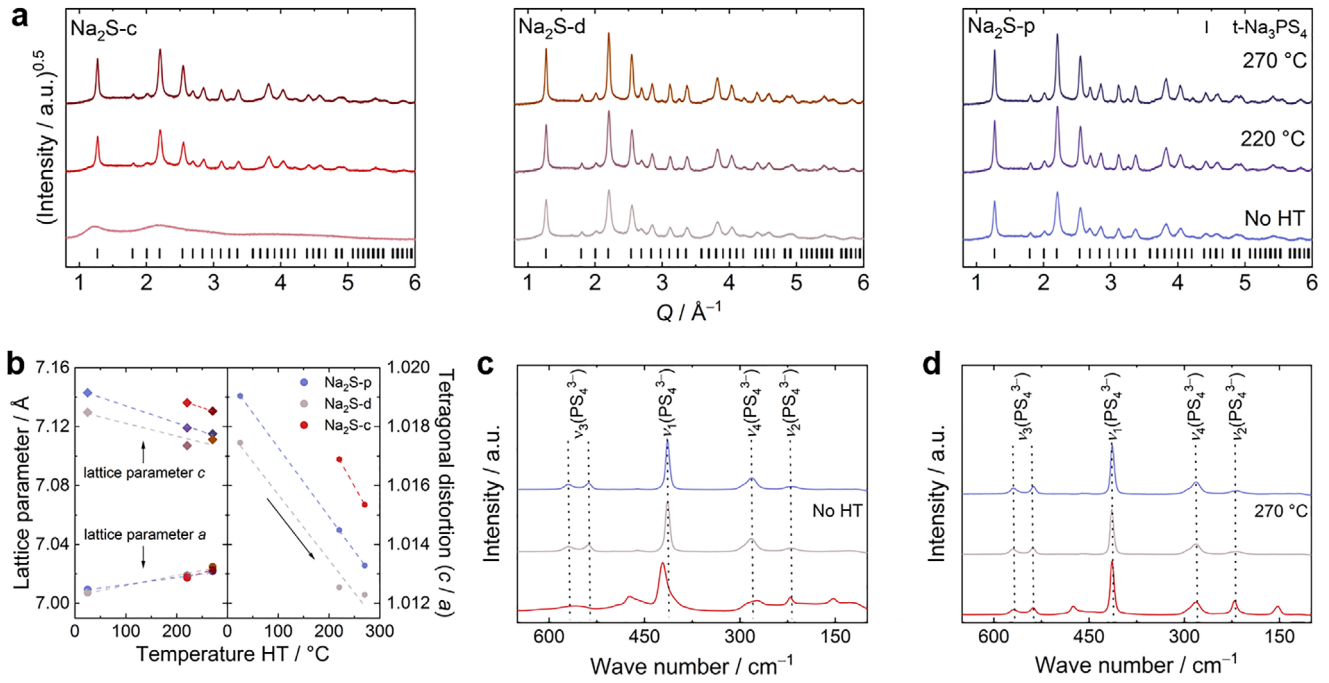

Figure 2. a) Diffraction patterns of tetragonal Na_3PS_4 (Bragg positions indicated) synthesized with Na_2S-c, Na_2S-d, and Na_2S-p, respectively, without and with HT at 220 or 270 °C. b) Evolution of lattice parameters depending on the heating procedure. c,d) Raman spectra of Na_3PS_4 made by Na_2S-c, Na_2S-d, and Na_2S-p, respectively, before and after HT at 270 °C.

peaks at BE = 159.8 eV. Polysulfides are detected in all samples between BE = [161.4, 161.8] eV, which contrasts with the Raman results.[43] This can be explained by trace amounts of Na_2S_x present on the surface of Na_2S-c and Na_2S-p. In the case of Na_2S-p, trace amounts of oxidation products might stem from brief atmospheric contact during the purification process.

In conclusion, Na_2S-c suffers from Na_2SO_x (particularly Na_2SO_3) while Na_2S-d contains Na_2S_x and trace amounts of Na_2SO_x. Na_2S-p is practically free from Na_2S_x and Na_2SO_x.

2.2. Influence of Na_2S Purity on the Synthesis of Na_3PS_4 and $Na_{2.85}P_{0.85}W_{0.15}S_4$

2.2.1. Synthesis of Na_3PS_4 with Different Na_2S Precursors

Na_3PS_4 was synthesized via a mechanochemical process similar to the route described by Nguyen et al.[13] XRD patterns of products obtained by three different synthesis conditions are shown in **Figure 2a**. Tetragonal Na_3PS_4 is received through mechanical milling when Na_2S-p or Na_2S-d is used as precursor. "Cubic" Na_3PS_4 is often obtained through mechanical milling, but the average crystal structure might depend on the milling parameters. For example, Hayashi et al. and Krauskopf et al. obtained "cubic" Na_3PS_4, while Nguyen et al. obtained tetragonal Na_3PS_4 by using similar synthesis parameters compared to this work.[13,14,24] For Na_2S-c, only amorphous material forms from which tetragonal Na_3PS_4 evolves after heat treatment (HT). Lattice parameters and tetragonal distortion (c/a ratio) (Figure 2b), obtained by Pawley fits, (S2) indicate no incorporation of oxygen in the crystalline phase since no crystalline Na_3PS_3O or lattice contraction is found.[44] The tetragonal distortion varies between samples and decreases upon sintering at 220 and 270 °C, underlining the discrepancy between local and global structure in mechanically milled Na_3PS_4.[24] Raman spectra of HT and non-HT Na_3PS_4 (Figure 2c,d) give insight into the local structure and reveal similar spectra for Na_2S-p and Na_2S-d independent of any HT. These are in accordance with literature.[17,45–48] The characteristic bands observed are ν_1 = 413, ν_3 = 538, and ν_3 = 570 cm^{-1}, ν_4 = 282 cm^{-1} and the weak ν_2 = 216 cm^{-1}. For Na_2S-c, after mechanical milling, a less defined spectrum is obtained. The characteristic ν_1 band shifts to 422 cm^{-1}, indicating the presence of Na_3PS_4 glass.[49,50] The ν_3 and ν_4 bands are less resolved and new bands at ν = {153, 474} cm^{-1} appeared. The ν = 474 cm^{-1} band strongly indicates the presence of polysulfide residues in the electrolyte.[27,33,34] After HT, the additional bands remain, but the spectrum is more defined, and crystalline Na_3PS_4 is clearly present. These findings support the XRD results.

XP spectra of S2p and P2p orbitals of Na_3PS_4 (**Figure 3**) give no evidence of SO_x groups in any electrolyte. This indicates that SO_x groups in Na_2S may be reduced during ball milling while oxygen binds with phosphorus. XPS further supports the Raman and XRD results. In the case of Na_2S-p and Na_2S-d, no change due to HT at 270 °C is observed, and no additional chemical reaction is triggered. The P2p and S2p peaks of PS_4^{3-} are observed at BE = {131.7, 163.1} eV, respectively. Polysulfides and PO_x species are present on the surface of all electrolytes, likely stemming from PO_x impurities (S1), off-stoichiometry in the P_4S_{10} precursor, and synthesis. In the case of Na_2S-c, changes in the P2p and S2p spectra occur after HT. The polysulfide peak shifts from BE = 162.7 to BE = 162.0 eV, which indicates the formation of

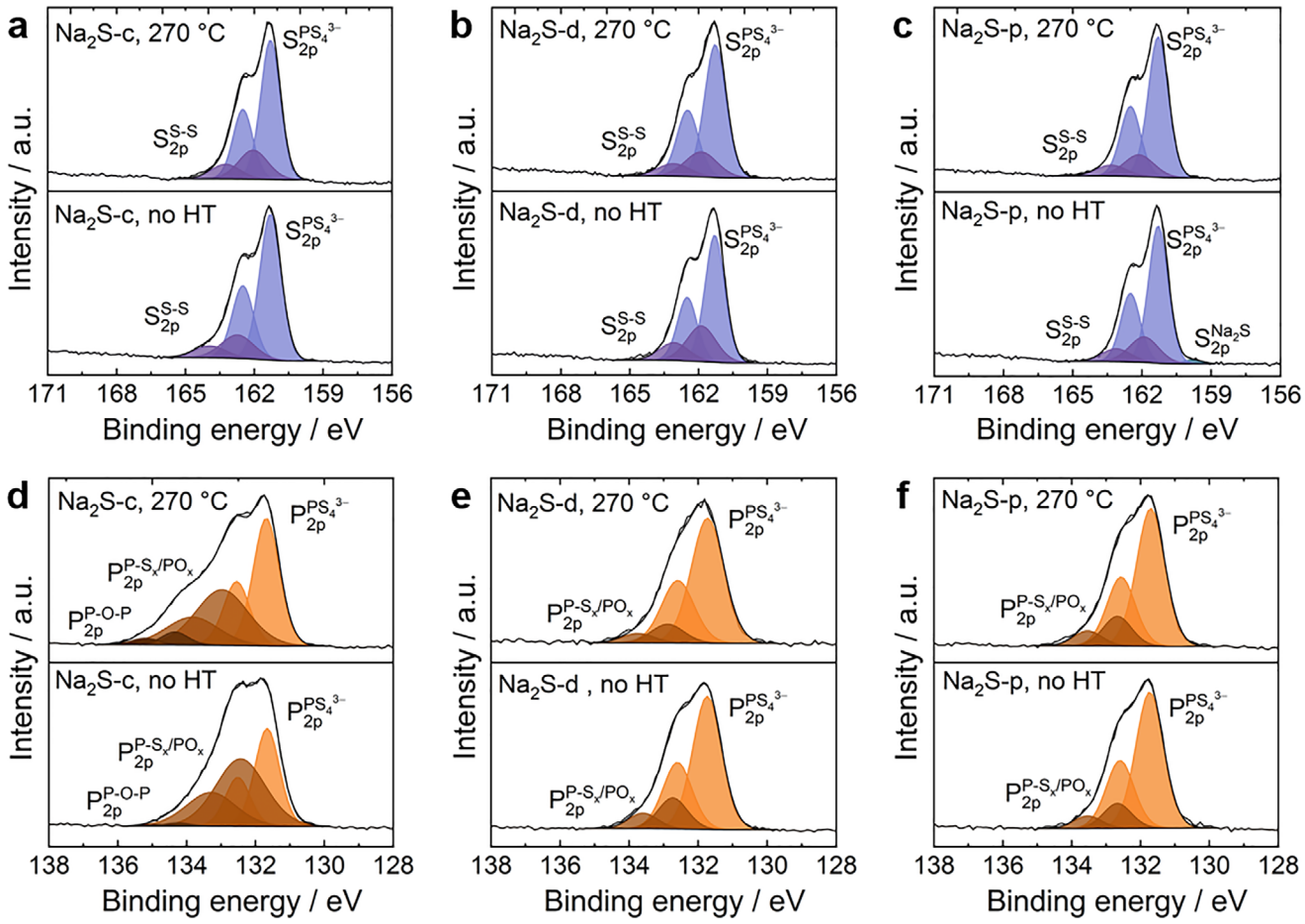

Figure 3. a–c) XP S2p and d,e) P2p spectra of Na_3PS_4 synthesized with Na_2S-c, Na_2S-d, and Na_2S-p, respectively, before and after HT at 270 °C. Material made with Na_2S-c undergoes further chemical reaction upon heating. A detailed explanation of the calibration process can be found in the Supporting Information. For signals incorporating multiple species, an increased FWHM was used to regard the different BE.

shorter-chain polysulfides.[43] More severe changes are found in the P2p spectrum. Phosphorus species with very high BE are detected at BE = 134.3 eV, which could be attributed to species similar to $(NaPO_3)_n$ glasses.[51] This peak intensifies during HT from 1 to 9 atom%. Additionally, the PS_4^{3-} signal increases during HT from 42 to 56 atom%, while the broad peak associated with other PO_x and polysulfide species decreases from 57 to 35 atom% and shifts from BE = 132.4 to BE = 133.0 eV.

Analysis of the PDF allows the investigation of the local structure of both amorphous and crystalline materials. For all Na_3PS_4 samples heated at 270 °C, PDFs (**Figure 4**) indicate the same local structure, which can be attributed to tetragonal Na_3PS_4.[24,48] Na_2S-c leads to slightly lower intensities and more influence of Fourier termination ripples, affecting the overall PDF quality, and might indicate that the oxygen-containing impurity phase(s) causes the reduced data quality. In addition, a faster intensity decay is found as a function of the radial distance, suggesting a lower coherence in that sample. Nevertheless, no P—O bonds are observed, suggesting a low volume fraction, and in the cases of Na_2S-d and Na_2S-p, no impurities are observed, likely falling under the detection limit. To verify the presence of an amorphous side phase in Na_3PS_4 synthesized by Na_2S-c, a Rietveld refinement (S2) of a mixture with 10 wt.% LaB_6 was conducted. The refinement suggests 12.3 ± 0.1 wt.% LaB_6, indicating the presence of an amorphous phase (10 wt.%) in this Na_3PS_4 sample. This side phase likely contains the oxygen-containing species.

Concluding this section, the analytical data suggest that during synthesis oxygen from Na_2SO_x forms P—O bonds and that crystallization of Na_3PS_4 is hindered by impurities. HT is needed to assist the crystallization in the case of Na_3PS_4 synthesized by Na_2S-c. XPS might indicate further concentration of oxygen and formation of oxygen-rich phosphorus species during HT, but this could only be a surface phenomenon. XRD and PDF data indicate that there is no detectable incorporation of oxygen-containing $PO_xS_{4-x}^{3-}$ species in the crystalline Na_3PS_4 phase.

2.2.2. Effect of Na_2S Impurities on the Ionic Conductivity of Na_3PS_4

Nyquist plots of the conductivity data of Na_3PS_4 (**Figure 5**a–c) reveal the influence of the precursor quality on $\sigma(Na^+)$. Shimoda et al. demonstrated that synthesis of Na_3SbS_4 yields different $\sigma(Na^+)$ depending on which phase region is hit. The Na_3SbS_4

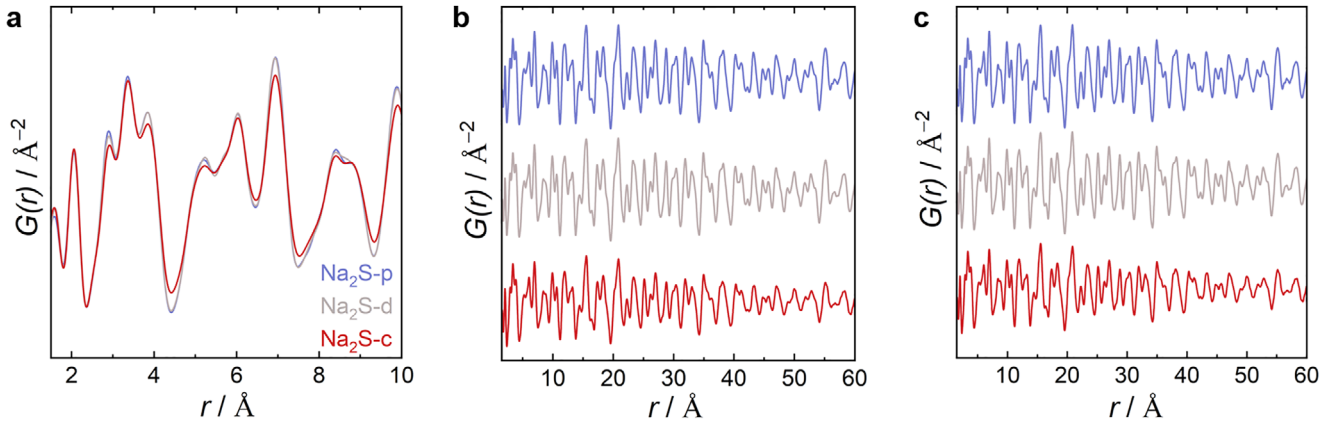

Figure 4. a–c) PDF of Na_3PS_4 (HT 270 °C) at different length scales synthesized with Na_2S-p, Na_2S-d, and Na_2S-c, respectively. The local structure is the same for all electrolytes. In (a), intensity discrepancies between the three Na_3PS_4 samples indicate a different fraction of amorphous phase(s). In (c), the faster decay of $G(r)$ in Na_2S-c indicates a smaller coherence length. PDF refinements can be found in the Supporting Information (S8).

phase (Na_3PS_4 in the case of this study) is a point phase in the ternary Na, S, Sb (P) phase diagram. The Na_2S impurities are likely to affect the obtained phase field, which would explain differences in $\sigma(Na^+)$.[52] Na_2S-c leads to the lowest $\sigma(Na^+)$, especially without HT. With increasing HT temperature, $\sigma(Na^+)$ improves significantly, yet $\sigma(Na^+) < 0.04$ mS cm^{-1}. The usage of Na_2S-p and Na_2S-d yields different results. Here, mechanical milling alone is sufficient for $\sigma(Na^+) > 0.1$ mS cm^{-1}. We attribute this to the successful formation of partially crystalline Na_3PS_4 without any HT. Na_3PS_4 synthesized by Na_2S-p or Na_2S-d reaches a maximum $\sigma(Na^+) = 0.14$ and $\sigma(Na^+) = 0.17$ mS cm^{-1}, respectively, after HT at 220 °C. HT at 270 °C leads to a

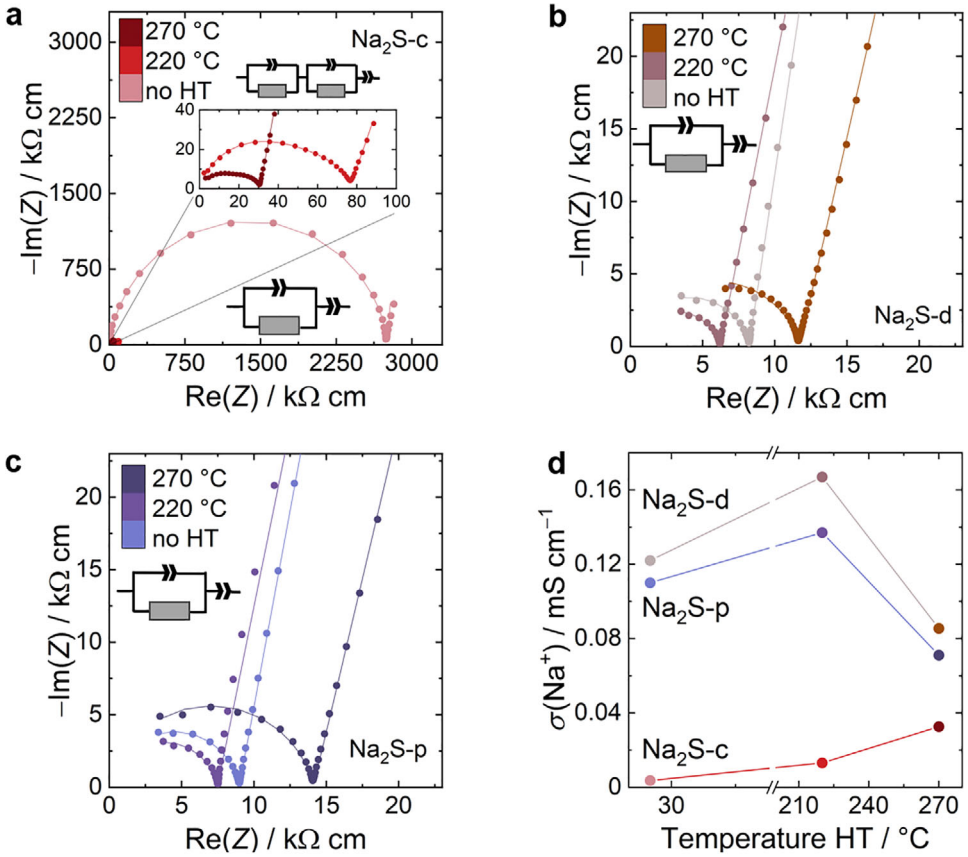

Figure 5. a–c) Nyquist plots of conductivity data of Na_3PS_4 synthesized with Na_2S-c, Na_2S-d, and Na_2S-p before and after HT at 220 or 270 °C. d) Comparison of $\sigma(Na^+)$ of Na_3PS_4 samples. In (a-c), the symbols represent measured data while the lines indicate the impedance fit. For fitting, an RQ circuit combined with a Q element was used. For Na_3PS_4 synthesized with Na_2S-c at 220 or 270 °C, another RQ circuit was added.

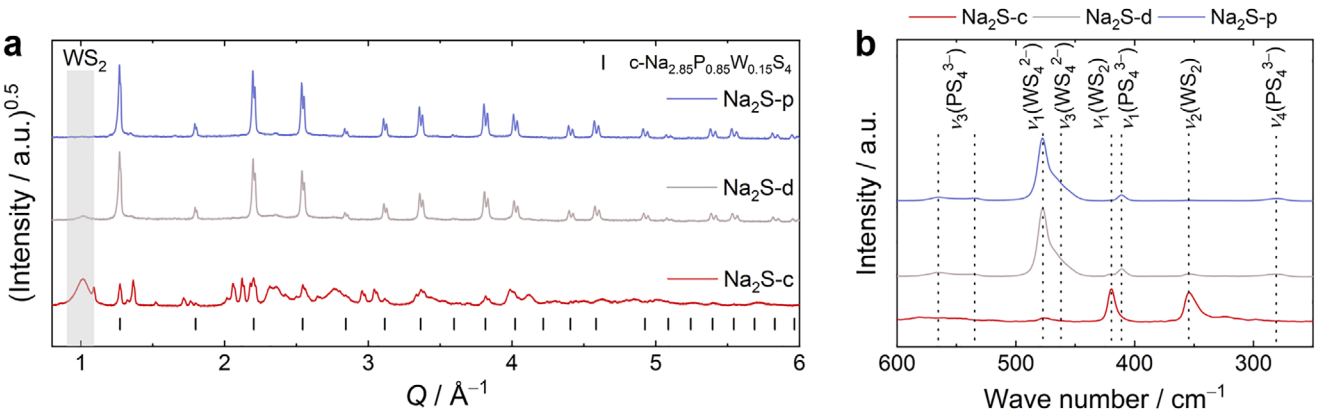

Figure 6. a) Diffraction patterns and b) Raman spectra of $Na_{2.85}P_{0.85}W_{0.15}S_4$ synthesized with Na_2S-c, Na_2S-d, and Na_2S-p, respectively. While $Na_{2.85}P_{0.85}W_{0.15}S_4$ was synthesized successfully with Na_2S-d and Na_2S-p, Na_2S-c leads to unsuccessful synthesis. Rietveld refinements and Pawley fits can be found in the Supporting Information (S4). Bragg positions of cubic $Na_{2.85}P_{0.85}W_{0.15}S_4$ are indicated.

reduction of $\sigma(Na^+)$. This behavior might be explained by reduction of the defect concentration, which would impair $\sigma(Na^+)$. Regarding the influence of HT on $\sigma(Na^+)$ of Na_3PS_4, literature is ambiguous. Krauskopf et al. and Nguyen et al. found little impact, while Hayashi et al. deem HT necessary.[13,14,24] Like the aforementioned discrepancies between average crystal structure, different HT behavior might very well be explained by different synthesis parameters. Especially milling parameter vary between nearly all publications. Hayashi et al. obtained amorphous Na_3PS_4 after prolonged mechanical milling, making HT necessary to obtain partially crystalline Na_3PS_4.[14] In contrast, Krauskopf et al. and Nguyen et al. obtained partially crystalline Na_3PS_4 after mechanical milling, which explains the higher $\sigma(Na^+)$ without HT.[13,24] With the same parameter set, the behavior clearly depends on the impurity content. Significant fractions of oxygen impurities (as in Na_2S-c) make HT necessary to obtain any significant $\sigma(Na^+)$, while Na_3PS_4 made with pure or Na_2S_x contaminated Na_2S (Na_2S-p and Na_2S-d, respectively) does not necessarily require additional HT. In fact, temperatures approaching 300 °C can decrease $\sigma(Na^+)$. Interestingly, Na_2S-d enables the highest $\sigma(Na^+)$ for Na_3PS_4 (Figure 5d) despite the presence of impurities. Confusing at first, we explain this by the formation of sodium-deficient and sulfur-rich Na_3PS_4 through excess sulfur from Na_2S_x species. Na-deficient Na_3PS_4 would result in more V_{Na^+}, increasing $\sigma(Na^+)$. The same behavior is found by Shimoda et al. for Na_3SbS_4, where $\sigma(Na^+)$ varies strongly depending on the stoichiometry, being either sodium-rich or sulfur-rich.[52]

2.2.3. Na_2S Purity Effects on the Synthesis of $Na_{2.85}P_{0.85}W_{0.15}S_4$

The synthesis of $Na_{2.85}P_{0.85}W_{0.15}S_4$ shows a different behavior and sensitivity regarding Na_2S_x and SO_x impurities. The XRD patterns (**Figure 6a**) demonstrate an unsuccessful synthesis when Na_2S is significantly contaminated with Na_2SO_x (Na_2S-c). The resulting product is a mixture of mainly WS_2, Na_3PS_4, and Na_3POS_3.[14,44,47] Rietveld refinement suggests a Na_3POS_3 content of 70.3 ± 0.5 mol% which would imply 15.6 ± 0.1 mol% Na_2SO_3 in Na_2S, assuming complete reaction of Na_2SO_3 to Na_3POS_3. This is in line with the Rietveld refinement of Na_2S, which indicates a Na_2SO_3 content of 13.5 ± 4.5 mol%. Now, the oxygen impurities seem to be incorporated in a crystalline phase, and no highly oxygenated phosphorous species at high BE are observed. This contrasts the findings for Na_3PS_4 synthesized at lower temperatures. Nakajima et al. reported a crystallinity degree approaching 100% for mechanically milled Na_3PS_4 upon heating beyond 400 °C.[53] This might also apply to $PO_xS_{4-x}^{3-}$ anions like in Na_3POS_3 and $Na_3PO_2S_2$, which have already been reported.[44,54]

In contrast, Na_2S-p and Na_2S-d lead to the successful formation of $Na_{3-x}P_{1-x}W_xS_4$, but in case of Na_2S-d, residual WS_2 is detected. Off-stoichiometry caused by its Na_2S_x impurities might cause the lower solubility of WS_4^{2-}. Therefore, we conclude that pure precursor phases are likely to be necessary for the formation of $Na_{3-x}P_{1-x}W_xS_4$.

The Raman spectra (Figure 6b) are consistent with these findings. In the case of Na_2S-c, only trace amounts of WS_4^{2-} are detected, while strong bands which originate from WS_2 are observed. Strong WS_4^{2-} bands are observed for material synthesized with Na_2S-p and Na_2S-d. In accordance to the diffraction patterns, weak WS_2 signals are detected in case of Na_2S-d.[17,47,55,56]

The XPS measurements (**Figure 7a**) also reveal WS_2 in the material prepared from Na_2S-d and Na_2S-c at BE = 32.4 eV, which aligns well with literature,[57] while Na_2S-p enables full oxidation of WS_2 to WS_4^{2-} which we found located at BE = 33.5 eV. The weak Na2p signal in the case of Na_2S-c can be explained by uneven WS_2 distribution with accumulation on the particle surface. After sputtering (S1), the Na1s signal strengthens, indicating an accumulation of WS_2 at the particle surface, which fits the black color of the product mixture.

The S2p spectra (Figure 7b) are similar to Na_3PS_4 with no observable individual signal for WS_4^{2-} and no shift of the P/WS_4^{2-} signal. Only Na_2S-c leads to differences. The PS_4^{3-} peak in the S2p spectrum is broadened and likely also contains contributions from POS_3^{3-}. The polysulfide peak is shifted to higher BE due to WS_2.[57] A XP spectrum of WS_2 can be found in the Supporting Information (S1).

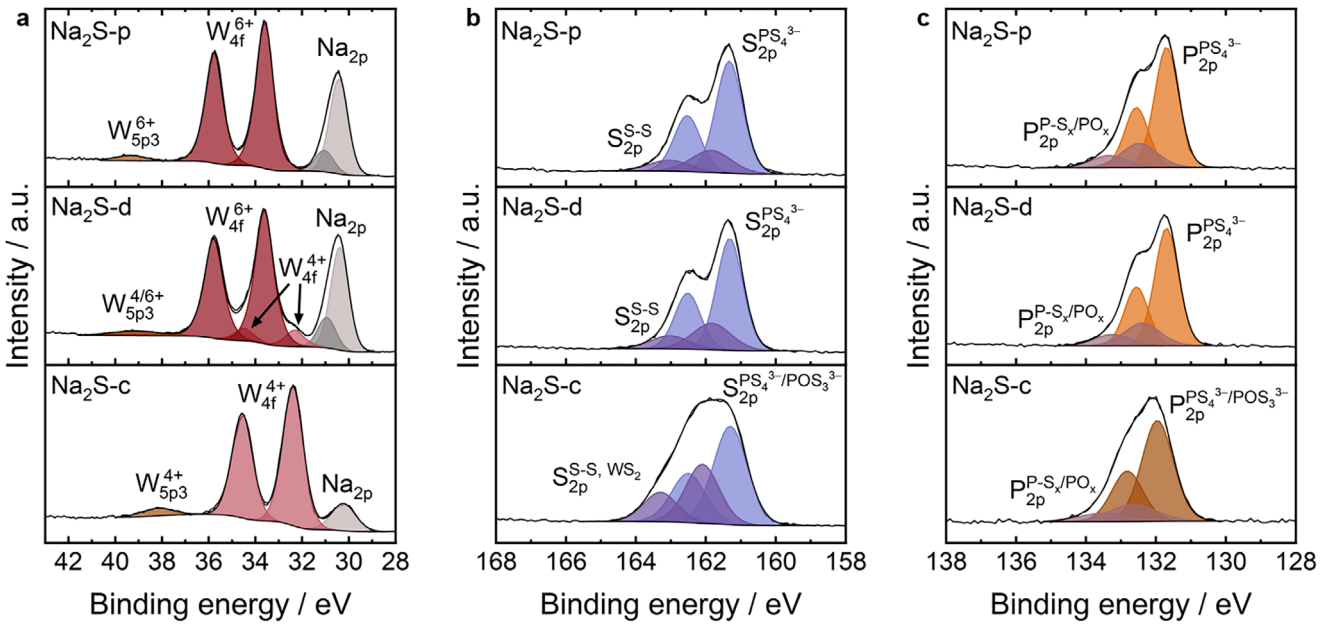

Figure 7. a–c) W4f, S2p and P2p spectra of $Na_{2.85}P_{0.85}W_{0.15}S_4$ synthesized by Na_2S-c, Na_2S-d and Na_2S-p. Only the use of pure Na_2S leads to complete formation of the WS_4^{2-} tetrahedra and no residual WS_2. For signals incorporating multiple species, increased FWHM was used to account for the different BE.

Differences are also observed in the P2p spectra (Figure 7c). While $Na_{2.85}P_{0.85}W_{0.15}S_4$ synthesized with Na_2S-p and Na_2S-d, shows similar P2p spectra as Na_3PS_4 with PS_4^{3-} located at BE = 131.7 eV. A broadened and shifted main peak can be observed for Na_2S-c. This peak includes PS_4^{3-} and POS_3^{3-} anions and is located at BE = 132.0 eV.

2.2.4. Influence of Impurities in Na_2S on the Ionic Conductivity of $Na_{2.85}P_{0.85}W_{0.15}S_4$

Both Na_2S-p and Na_2S-d enable high $\sigma(Na^+)$ = 14.7 and $\sigma(Na^+)$ = 9.7 mS cm^{-1}, respectively (**Figure 8a**). Na_2S-p enables 50% higher $\sigma(Na^+)$, which underlines how harmful impurities are for the formation of defined $Na_{2.85}P_{0.85}W_{0.15}S_4$ and the solubility of WS_4^{2-}.

To verify whether Na_2S_x (excess sulfur) or trace amounts of SO_x groups in Na_2S-d reduce $\sigma(Na^+)$, $Na_{2.85}P_{0.85}W_{0.15}S_4$ was additionally synthesized from Na_2S-p with 12.5% sulfur excess. Both Na_2S-d and Na_2S-p with excess sulfur result in a slight decrease in tungsten solubility (S4). Nevertheless, for Na_2S-p, $\sigma(Na^+)$ of $Na_{2.85}P_{0.85}W_{0.15}S_4$ is not affected significantly by the sulfur excess.

We observe that $\sigma(Na^+)$ correlates linearly with lattice parameter a in $Na_{3-x}P_{1-x}W_xS_4$ until $Na_{2.8}P_{0.8}W_{0.2}S_4$ is reached if synthesized with Na_2S-p (Figure 8b). $Na_{2.85}P_{0.85}W_{0.15}S_4$ synthesized with Na_2S-d falls out of this trend, indicating an additional effect besides incorporating less WS_4^{2-}. PDF data (Figure 8c,d) suggest the same local structure of $Na_{2.85}P_{0.85}W_{0.15}S_4$ regardless of selecting Na_2S-d or Na_2S-p as precursor. The small differences likely stem from Fourier termination ripples caused by the transformation of the total scattering data.

It seems that trace amounts of SO_x groups in Na_2S affect the formation of $Na_{2.85}P_{0.85}W_{0.15}S_4$ more severely than excess sulfur alone. The phase system is even more complex as in the case of Na_3PS_4 or Na_3SbS_4, and different kinds of impurities might affect the achieved stoichiometry of the electrolyte phase differently. Excess sulfur might also partially evaporate during HT, potentially reducing its effect on the stoichiometry. As in the case of Na_3PS_4, we did not observe clear evidence of incorporation of anions like POS_3^{3-} in the electrolyte phase. Impurities are likely to form a separate phase, but the Na_3POS_3 content is below the detection limit of XRD in the case of Na_2S-d.

Concluding this section, Na_2S free of Na_2SO_x is needed to obtain highly conductive $Na_{3-x}P_{1-x}W_xS_4$. While the formation of sulfur-rich Na_3PS_4 by Na_2S_x contaminations can be beneficial for $\sigma(Na^+)$, no beneficial effect for $Na_{2.85}P_{0.85}W_{0.15}S_4$ is observed. Na_2SO_x contaminations are detrimental for both electrolytes, Na_3PS_4 and $Na_{3-x}P_{1-x}W_xS_4$, but the synthesis of the latter is much more sensitive. While Na_3PS_4 formation/crystallization can be supported by HT, 13.5 mol% of Na_2SO_3 in Na_2S leads to complete failure of the $Na_{2.85}P_{0.85}W_{0.15}S_4$ synthesis.

While being out of the scope of this study, there are two other very important aspects to consider. When analyzing electrolyte stability against sodium metal anodes, we expect impurities to affect results significantly. Especially oxygen is reported to increase interface compatibility with sodium metal.[58–60] Thus, an amorphous, oxygen-containing phase would heavily affect studies conducted with Na_3PS_4. Preliminary results of the stability of Na_3PS_4, $Na_{2.95}P_{0.95}W_{0.05}S_4$, and $Na_{2.8}P_{0.8}W_{0.2}S_4$ against sodium metal can be found in the Supporting Information (S14). In agreement with an early study by Wenzel et al., Na_3PS_4 shows fast degradation due to formation of a mixed-conducting interphase (MCI).[61] With rising tungsten content, the instability against sodium metal is growing. Also, the performance of Na-S cells is expected to be reduced by insulating Na_2SO_x, especially when accumulated on the particle surface (Na_2S-c).

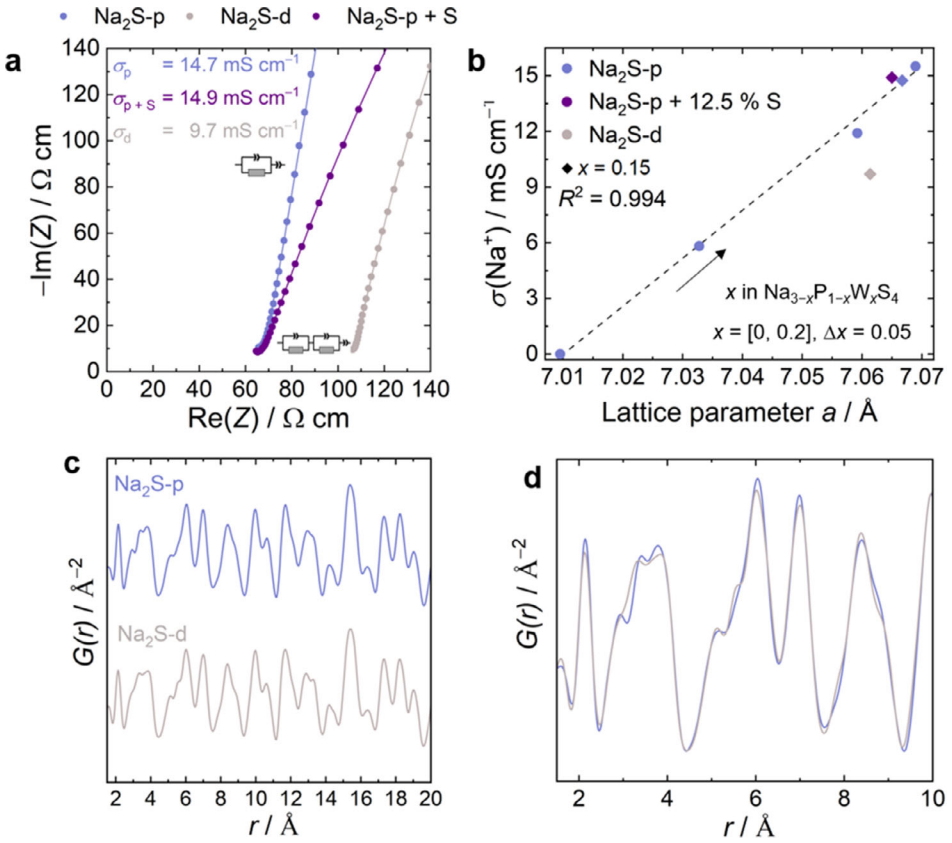

Figure 8. a) Nyquist representation of impedance data of $Na_{2.85}P_{0.85}W_{0.15}S_4$ synthesized with Na_2S-p (+ 12.5% S) and Na_2S-d. b) Correlation of $\sigma(Na^+)$ and a. c) PDF of $Na_{2.85}P_{0.85}W_{0.15}S_4$ synthesized with Na_2S-p and Na_2S-d. d) Comparison of the two PDF. In (a), Na_2S-d or excess sulfur leads to an additional impedance contribution, likely stemming from constriction and/or increased $\sigma(e^-)$ by WS_2 (S13). For fitting, an RQ circuit combined with a Q element was used for Na_2S-p, while another RQ circuit was added for Na_2S-d and Na_2S-p + 12.5% sulfur excess, to regard the additional impedance contribution.

In the supporting information, a side investigation about the reaction temperature (e.g., short sintering at moderate temperatures) and sulfur deficiency during synthesis is discussed. Both, sulfur deficiency or insufficient HT, reduce the formation of WS_4^{2-} and $\sigma(Na^+)$.

2.3. Expanding the $Na_{3-x}P_{1-x}P_{1-x}W_xS_4$ Family – Enabling 20 mS cm^{-1} Electrolytes

2.3.1. Tungsten Solubility in $Na_{3-x}P_{1-x}W_xS_4$

Previous work on the $Na_{3-x}P_{1-x}W_xS_4$ system investigated different tungsten concentrations and synthesis parameters. Reported electrolytes suffer from varying fractions of WS_2 residue at any tungsten concentration and unknown side phases beyond $x = 0.15$.[17,47] Tsuji et al. compared high temperature and mechanochemical syntheses with sintering at 220 °C, but found HT at 550 °C to be necessary to achieve high $\sigma(Na^+)$, similar to reported values by Fuchs et al.[17,47] Results of $Na_{2.9}P_{0.9}W_{0.1}S_4$ synthesized via mechanical milling and short sintering are shown in the Supporting Information (Chapter 4) and demonstrate that short HT at 375 °C for 4 h is not oxidizing all W^{4+} to W^{6+}, which explains the inferior value of $\sigma(Na^+)$. Figure 9a depicts XRD patterns of $Na_{3-x}P_{1-x}W_xS_4$ electrolytes ($x = [0, 0.35]$, $\Delta x = 0.05$) synthesized with Na_2S-p by a two-step heating process. All electrolytes below $x = 0.25$ show no residual WS_2, and only $Na_{2.7}P_{0.7}W_{0.3}S_4$ and $Na_{2.65}P_{0.65}W_{0.35}S_4$ suffer from significant fractions of WS_2 residue.

As the zoom in Figure 9b shows, the intensity of the $Na_{3-x}P_{1-x}W_xS_4$ 310 plane decreases with increasing tungsten content, becoming undetectable for $Na_{2.75}P_{0.75}W_{0.25}S_4$. The lattice parameter a (Figure 9c) is barely changing beyond $Na_{2.75}P_{0.75}W_{0.25}S_4$ as well. Additionally, small amounts of WS_2 residue appear in $Na_{2.75}P_{0.75}W_{0.25}S_4$, which altogether indicates the presence of a solubility limit of tungsten in $Na_{3-x}P_{1-x}W_xS_4$ at $x \approx 0.25$ (Figure 9d), at least for the precursor quality used in this work. The determined tungsten solubility is well beyond reported values for $Na_{3-x}P_{1-x}W_xS_4$ electrolytes, which suffer from WS_2 residue at any tungsten concentration.[17,47]

2.3.2. Ionic Conductivity of $Na_{3-x}P_{1-x}W_xS_4$ Electrolytes

Figure 10a,b shows conductivity data of the synthesized, cold-pressed $Na_{3-x}P_{1-x}W_xS_4$ electrolytes as a function of temperature and $\sigma(Na^+)$ at room temperature. With increasing

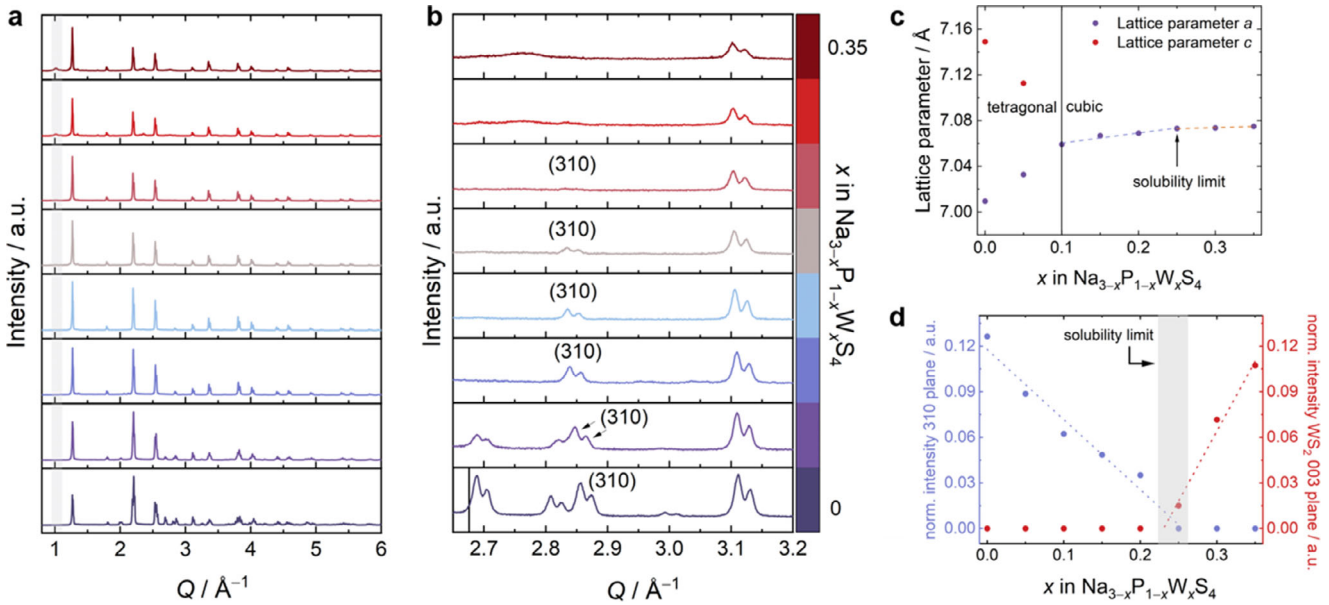

Figure 9. a) Diffraction patterns and b) enlargement of the 17–21 ° range of $Na_{3-x}P_{1-x}W_xS_4$ (x = [0, 0.35], Δx = 0.05). c) The evolution of lattice parameters of $Na_{3-x}P_{1-x}W_xS_4$ with rising tungsten content, and d) evolution of WS_2 precursor (marked grey in (a)) and the 310 plane of $Na_{3-x}P_{1-x}W_xS_4$. Pawley fits of $Na_{3-x}P_{1-x}W_xS_4$ and a W4f XP spectrum of $Na_{2.8}P_{0.8}W_{0.2}S_4$ can be found in the Supporting Information (S3).

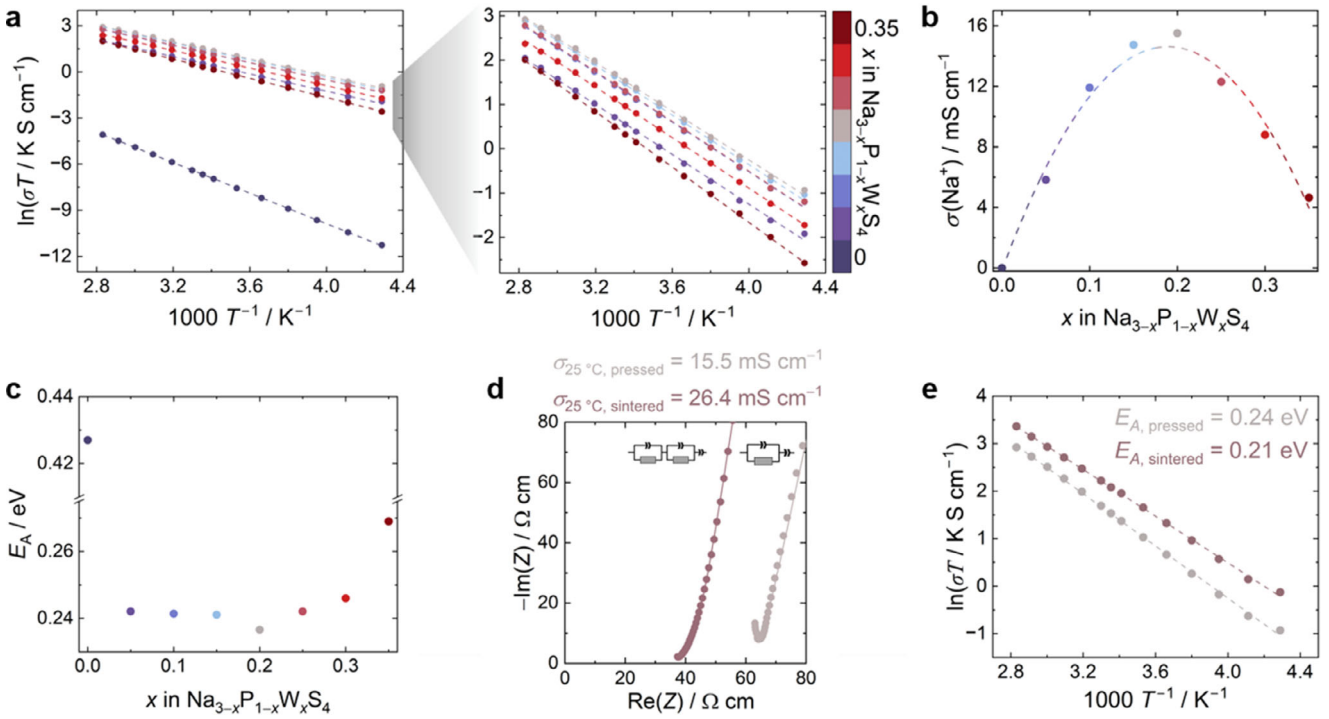

Figure 10. a) Arrhenius plots, b) $\sigma(Na^+)$ at 25 °C and c) E_A of $Na_{3-x}P_{1-x}W_xS_4$ (x = [0, 0.35], Δx = 0.05). d) $\sigma(Na^+)$ at 25 °C and e) E_A of cold-pressed and sintered $Na_{2.8}P_{0.8}W_{0.2}S_4$. For fitting, an RQ circuit combined with a Q element was used. For the sintered $Na_{2.8}P_{0.8}W_{0.2}S_4$ pellet, another RQ circuit was added to represent a small impedance contribution, likely stemming from the electrodes applied by high-temperature gold deposition. The virtually constant value of E_A = 0.24 eV over the solubility range in $Na_{3-x}P_{1-x}W_xS_4$ (x = [0, 0.25]) indicates that interaction of Na^+ with the host lattice does not change significantly. Differences in $\sigma(Na^+)$ likely stem from increasing concentration of sodium vacancies V_{Na^+}.

Table 1. Room temperature $\sigma(Na^+)$, $D(Na^+)$ and $\mu(Na^+)$ of $Na_{3-x}P_{1-x}W_xS_4$ ($x = [0, 0.25]$, $\Delta x = 0.05$) synthesized by Na_2S-p under the assumption of $f = 1$. Lattice parameters obtained by Pawley fits and the nominal Na^+ content were used to obtain n.

Electrolyte	$\sigma(Na^+)$/mS cm^{-1}	10^{28} n/m^3	D/m^2 s^{-1}	μ/m^2 V^{-1} s^{-1}
Na_3PS_4, 570 °C	0.00425	1.71	$3.98 \cdot 10^{-15}$	$1.55 \cdot 10^{-13}$
Na_3PS_4, 220 °C	0.137	1.71	$1.28 \cdot 10^{-13}$	$4.98 \cdot 10^{-12}$
$Na_{2.95}P_{0.95}W_{0.05}S_4$	5.82	1.68	$5.55 \cdot 10^{-12}$	$2.16 \cdot 10^{-10}$
$Na_{2.9}P_{0.9}W_{0.1}S_4$	11.9	1.65	$1.16 \cdot 10^{-11}$	$4.52 \cdot 10^{-10}$
$Na_{2.85}P_{0.85}W_{0.15}S_4$	14.7	1.62	$1.45 \cdot 10^{-11}$	$5.65 \cdot 10^{-10}$
$Na_{2.8}P_{0.8}W_{0.2}S_4$	15.5	1.59	$1.56 \cdot 10^{-11}$	$6.07 \cdot 10^{-10}$
$Na_{2.8}P_{0.8}W_{0.2}S_4$, sintered	26.4	1.59	$2.66 \cdot 10^{-11}$	$1.04 \cdot 10^{-9}$
$Na_{2.75}P_{0.75}W_{0.25}S_4$	12.3	1.55	$1.27 \cdot 10^{-11}$	$4.94 \cdot 10^{-10}$

WS_4^{2-} concentration, $\sigma(Na^+)$ increases and reaches a maximum in the range $x = [0.15, 0.2]$, with $Na_{2.8}P_{0.8}W_{0.2}S_4$ achieving $\sigma(Na^+) = 15.5$ mS cm^{-1}. Na_3PS_4 synthesized with the same high temperature procedure, shows $\sigma(Na^+) = 4.25$ µS cm^{-1}, roughly 3600 times less.

When reaching the solubility limit of tungsten, $\sigma(Na^+)$ decreases, especially for nominal tungsten substitutions of $x \geq 0.3$. The activation energy (E_A) decreases abruptly from $E_A = 0.43$ eV in Na_3PS_4 to $E_A = 0.24$ eV in $Na_{3-x}P_{1-x}W_xS_4$ ($x = [0.05, 0.25]$) and increases for higher tungsten contents (Figure 10c). For tetragonal Na_3PS_4 synthesized by high temperature synthesis, high E_A and low $\sigma(Na^+)$ are in line with reported values by Hayashi et al. as well as Jansen and Henseler. The high E_A likely incorporates the V_{Na^+} formation energy of stoichiometric Na_3PS_4 due to a lack of unoccupied Na sites.[14,52,62] In fact, low $\sigma(Na^+)$ and high E_A can be an indicator for the formation of highly stoichiometric Na_3PS_4.

For $Na_{3-x}P_{1-x}W_xS_4$, the nearly constant $E_A = 0.24$ eV over a wide substitution range indicates that the increasing $\sigma(Na^+)$ stems from higher V_{Na^+} concentrations and not from further changes in interaction of Na^+ with the host lattice. This result contrasts Fuchs et al., who describe a linear decrease in E_A with rising WS_4^{2-} content.[17] For $Na_{2.8}P_{0.8}W_{0.2}S_4$, sintering increases $\sigma(Na^+)$ from $\sigma(Na^+) = 15.5$ to $\sigma(Na^+) = 26.4$ mS cm^{-1} while E_A drops to $E_A = 0.21$ eV (Figure 10d,e), likely caused by structural relaxation of grain boundaries and grain growth.

The diffusion coefficient $D(Na^+)$ can be calculated from the experimentally obtained $\sigma(Na^+)$ with the Nernst-Einstein Equation (Equation 1) if the correlation factor f is assumed to be $f = 1$, with the Boltzmann constant k_B, the temperature $T = 298$ K, the number of Na^+ per volume n and the charge of Na^+ $q = 1.602\ 10^{-19}$ C.

$$D(Na^+) = \frac{\sigma(Na^+) k_B T}{n q^2} \quad (1)$$

The mobility $\mu(Na^+)$ describes the drift velocity of Na^+ under the influence of an electric field and is depicted in Equation (2).

$$\mu(Na^+) = \frac{Dq}{k_B T} \quad (2)$$

Table 1. displays $D(Na^+)$ and $\mu(Na^+)$ of $Na_{3-x}P_{1-x}W_xS_4$ ($x = [0, 0.25]$, $\Delta x = 0.05$). Electrolytes with $x > 0.25$ were not regarded since side phases are likely to influence $\sigma(Na^+)$ and XRD data indicates a discrepancy between nominal and real tungsten content in $Na_{3-x}P_{1-x}W_xS_4$ if $x > 0.25$.

2.4. Synthesis Recommendations for Na_3PS_4 and $Na_{3-x}P_{1-x}W_xS_4$ Electrolytes

On the basis of our findings, we come to the following recommendations:

1) The strong impact of impurities in Na_2S calls for strict quality control before synthesis. Otherwise, unexpected behavior renders the comparison of different materials challenging. *E.g.*, even with precise weighing of Na_2S, Na_2S_x impurities can enforce sulfur-rich states, which boost $\sigma(Na^+)$ for Na_3PS_4.
2) To achieve the highest $\sigma(Na^+)$ for $Na_{3-x}P_{1-x}W_xS_4$ electrolytes, Na_2S purification is necessary, *e.g.*, by H_2, to remove all SO_x groups. Even small amounts of Na_2SO_x significantly reduce $\sigma(Na^+)$.
3) While Na_3PS_4 benefits only from sintering at low temperatures, $Na_{3-x}P_{1-x}W_xS_4$ requires high temperature synthesis to fully oxidize WS_2.

3. Conclusion

This work highlights the impact of notoriously present impurities in precursor Na_2S on the synthesis of Na_3PS_4 and $Na_{3-x}P_{1-x}W_xS_4$ solid electrolytes. We identified specific impurities in Na_2S, investigated their impact on the electrolyte synthesis, and used H_2 reduction for the purification of commercial Na_2S. While Na_2S_x as impurity can be beneficial for the synthesis of Na_3PS_4, only high-purity Na_2S leads to a complete tungsten incorporation in $Na_{3-x}P_{1-x}W_xS_4$, i.e., a homogeneous solid solution, and the highest $\sigma(Na^+)$. SO_x-related impurities in Na_2S are detrimental in both cases. We demonstrate high tungsten solubility in $Na_{3-x}P_{1-x}W_xS_4$ of up to $x \approx 0.25$ and an optimal tungsten substitution effect on $\sigma(Na^+)$ in the range $x = [0.15, 0.2]$. The highest $\sigma(Na^+)$ we achieved is $\sigma(Na^+) = 26.4$ mS cm^{-1} for $Na_{2.8}P_{0.8}W_{0.2}S_4$ in sintered pellets. To the best of our knowledge, this is the highest $\sigma(Na^+)$ in this electrolyte system reported so far, underlining the potential of this class of solid electrolytes.

Further work is needed to determine impurity thresholds to formulate quantitative purity requirements. Additionally, the

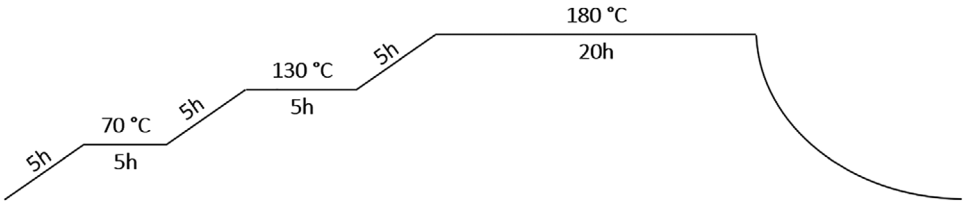

Figure 11. Heating procedure for drying Na_2S.

influence of P_4S_{10} purity needs to be investigated, which might further increase the $\sigma(Na^+)$ of $Na_{3-x}P_{1-x}W_xS_4$ electrolytes. Regarding the cell concepts, the influence of impurities on the interface stability against sodium metal and the performance impact on Na-S cells needs to be studied.

4. Experimental Section

Purification of Na_2S: $Na_2S \bullet x\ H_2O$ (Sigma–Aldrich, purity ≥ 60%, scales) was ground in an agate mortar to a fine yellow-orange powder, dried under dynamic vacuum (**Figure 11**), and transferred into a glovebox ($p(O_2)/p < 0.1$ ppm, $p(H_2O)/p < 1.5$ ppm).

The resulting light yellow and dried Na_2S was again ground in an agate mortar, loaded in an Al_2O_3 vessel, transported inside an airtight container to an argon-flushed quartz glass tube furnace (≈1 m in length and ≈4 cm in diameter), and transferred under argon counter flow. The gas flow was changed to 100 sccm H_2, and after 30 min of waiting, the heating program (**Figure 12**) was started.

Afterward, the reaction vessel was quickly transferred to an airtight vessel, which was evacuated to guarantee as little recontamination as possible during transfer to a glove box. The total atmosphere exposure was ≈15 s. Inside the glove box, the grey top layer of the sintered Na_2S body was removed. The resulting white Na_2S (Na_2S-p) was ground and used for analysis and synthesis. Na_2S (Na_2S-d), which was only dried under vacuum, was also used for analysis and synthesis.

Synthesis of Na_3PS_4 and $Na_{3-x}P_{1-x}W_xS_4$: Na_3PS_4 electrolytes were synthesized by a mechanochemical approach similar to routes reported in literature.[13] In a glovebox, 2 g of a stochiometric mixture of Na_2S (purified/dried/commercial (ThermoFisher, anhydrous, 95%, 96.26% according to Lot: R28H003)) and P_4S_{10} (Sigma-Aldrich, 99%) were filled in a 45 mL ZrO_2 jar (Fritsch) together with 10 ZrO_2 balls (Fritsch, $d = 10$ mm, $m = 3$ g). The ZrO_2 jar was closed and placed in a planetary micro mill (Pulverisette 7 premium line, Fritsch) outside the glovebox. The mixture was milled at 200 rpm for 2 min, followed by 6 cycles of milling at 600 rpm for 15 and 5 min resting for heat dissipation. After milling, the jar was opened in a glove box to collect the Na_3PS_4 electrolyte (beige color for Na_2S-p and Na_2S-d, yellow for Na_2S-c). For HT, the Na_3PS_4 samples were heated within 2 h to 220 or 270 °C and sintered at that temperature for 2 h under argon atmosphere. All Na_3PS_4 samples had a beige color after HT.

$Na_{3-x}P_{1-x}W_xS_4$ electrolytes were synthesized by a combination of mechanical milling and high-temperature reaction. The milling procedure was the same as for Na_3PS_4 with stochiometric mixtures of Na_2S (purified/dried/commercial (ThermoFisher, anhydrous, 95%, 96.26% according to Lot: R28H003)), P_4S_{10} (Sigma–Aldrich, 99%), S (Acros Organics, 99.999%), and WS_2 (chemPUR, 99.8%). The heating procedure is depicted in **Figure 13** and was conducted under argon atmosphere.

After milling, the electrolytes obtained were brown, and yellow-orange after HT. Higher tungsten concentrations resulted in darker colors. Na_2S-c resulted in a black product while Na_2S-d led to a slightly yellower electrolyte. For Na_2S-p with 12.5% sulfur excess, no color change compared to the synthesis with Na_2S-p was observed. Na_3PS_4, obtained by high-temperature synthesis, was white.

X-Ray Diffraction (XRD): For X-ray diffraction measurements of Na_2S, PANanalyticals Empyrean with a spinning sample holder was used, and the samples were kept under argon atmosphere with Kapton foil. A 2Θ range of 10–75 ° was analyzed with a step size of 0.013° with 150 s per step. The utilized radiation was the Cu-$K_{\alpha 1}$ line.

For X-ray diffraction measurements of the electrolytes and WS_2, powders were measured in a sealed glass capillary ($d = 0.5$ mm) with a PANanalyticals Empyrean. A 2Θ range of 5–40 ° was analyzed with a step size of 0.0072° with 200 s per step. The utilized radiation was the Mo-$K_{\alpha 1,2}$ line. For $Na_2S \bullet x\ H_2O$, a spinning sample holder was used, like for measurements with the Cu source.

X-Ray Photoelectron Spectroscopy (XPS): For the XPS analysis, a PHI5000 Versa Probe II system from Physical Electronics Inc was used. The sample powders were compacted into cylindrical Teflon cups ($d_{inner} = 3$ mm) with a stainless-steel pressing tool. The cups were fixed to the sample holder using nonconductive adhesive tape, and samples were transferred under argon atmosphere. For XPS analysis, monochromatic Al-K_α radiation (1486.6 eV) was utilized, and the X-ray source was operated at a power of 50 W and a voltage of 15 kV. The analysis spot diameter was 200 µm, and an analyzer pass energy of 55 eV was selected. A dual beam charge neutralization (combination of an ion and a low-energy electron beam) was utilized during measurements. For data evaluation, CasaXPS (Casa Software Ltd) was used, and the spectra were calibrated in relation to the C1s signal of adventitious carbon (BE = 284.8 eV), followed by a second calibration. Shirley background and common fitting restrictions were used for signal fitting. For tungsten, a GL60 line shape was applied. Peaks including multiple species (polysulfides, PO_x species) have increased FWHM constraints to regard similar but different BE.

A detailed explanation of the calibration process can be found in the Supporting Information.

Electrical Impedance Spectroscopy (EIS): For cold-pressed samples, electrolyte powders were compacted in a press cell setup ($d = 10$ mm) between stainless-steel stamps at 375 MPa for 3 min. EIS measurements were conducted with a VMP-300 potentiostat from Biologic, and a stack pressure of ≈70 MPa was applied. The frequency range was 7 or 3 MHz to 100 mHz, and the applied amplitude was 10 mV. Measurements were

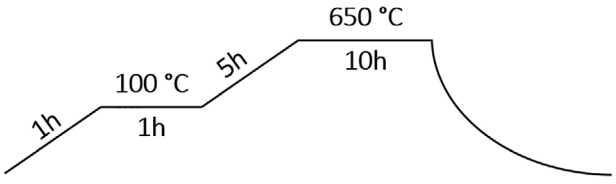

Figure 12. Heating procedure of the Na_2S purification. The intermediate heating step at 100 °C allows removal of residual moisture in the oven.

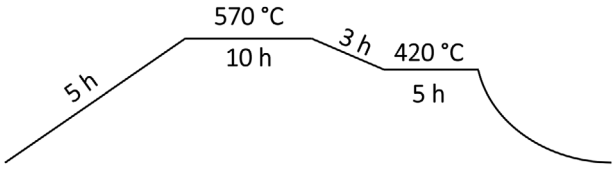

Figure 13. Heating procedure for the synthesis of $Na_{3-x}P_{1-x}W_xS_4$ ($x = [0, 0.35]$, $\Delta x = 0.05$) electrolytes.

conducted in a controlled environment at $T = 25$ °C. For comparing the effect of sintering, $Na_{2.8}P_{0.8}W_{0.2}S_4$ was isostatically pressed at 375 MPa for 45 min and sintered at 400 °C for 30 min. The densified pellet was then polished down to P4000 SiC polishing paper, and ≈200 nm thick gold electrodes were deposited via thermal vaper deposition on both sides. The pellet dimensions were $d_{pellet} \approx 7.5$ mm, $d_{Au} = 4.5$ mm, and the pellet thickness was 2.0 mm.

Temperature-dependent EIS measurements were conducted with a VMP-300 potentiostat and LabEvent L C/20/40/3 climate chambers from Weiss in a temperature range of −40–80 °C.

To reduce the impact of artifacts caused by setup inductivity, the measurement setup was measured in a short-circuited and open state for calibration. Compensation was made with the EC-Lab software from Biologic. Impedance fitting was conducted in the Relaxis software from rhd Instruments in a frequency range of up to 3 MHz down to 10 kHz for $Na_{3-x}P_{1-x}W_xS_4$, depending on the temperature. For Na_3PS_4, the frequency range was 7 MHz down to 50 Hz. For Na_3PS_4 synthesized by Na_2S-c and mechanical milling, the frequency range was extended to 10 Hz due to different time constants of the amorphous electrolyte. The Kramers-Kronig relation was checked to assure sufficient data quality of the chosen frequency range. The semi-circle stemming from the bulk and grain boundary contribution was often barely resolved. Nevertheless, RQ elements were used for fitting to attribute effects on the blocking tale at high/medium frequencies. The fits cannot and were not used to obtain any bulk/grain boundary capacities.

Raman Spectroscopy: The Raman spectroscopy measurements were conducted with a Brukers Senterra device equipped with a 532 nm laser. The samples were measured as powder and were sealed under argon atmosphere. For Na_2S, the spectral range was $\nu = [80, 4450]$ and $\nu = [51, 1550]$ cm^{-1} for $Na_{3-x}P_{1-x}W_xS_4$ ($x = \{0, 0.15\}$). The laser power was 2 mW. Multiple spots per sample were measured, and OPUS V. 7 was used for data collection.

Fourier-Transform Infrared Spectroscopy (FTIR): The FT-IR spectra of Na_2S were recorded with a ThermoFisher Scientific iD5 ATR spectrometer in a range of $\nu = [550, 4000]$ cm^{-1} in argon atmosphere. Na_2S was pressed in the pulver tip, and 96 scans per measurement were conducted.

Pair Density Function (PDF): Total scattering data were collected using a Stoe STADI P diffractometer with Ag Kα1 radiation ($\lambda = 0.55941$ Å) and a Ge (111) monochromator. Measurements were carried out in Debye-Scherrer geometry with four Dectris MYTHEN2 1K detectors. The samples were enclosed in sealed glass capillaries and measured for 24 h. Raw data were processed using PDFgetX3,[63] applying a Q-range cutoff at Qmax = 17 $Å^{-1}$. Small-box modeling was performed using PDFgui.[64] The analysis procedure followed the approach of Krauskopf et al.[24] PDF fitting was carried out in two R-ranges: 1.5–5 and 5–20 Å, separately. For both ranges, the scale factor, lattice parameters, correlated motion factor, atomic positions, and atomic displacement parameters were refined.

Supporting Information

Supporting Information is available from the Wiley Online Library or from the author.

Acknowledgements

The authors thank Sebastian L. Benz for fruitful discussions regarding XPS analysis and Elisa Monte for designing the ToC image. F.S., D.W., W.G., A.B., and J.J. thank the German Federal Ministry of Research, Technology, and Space (BMFTR) for funding within HiPoBat (03XP0611E).

Open access funding enabled and organized by Projekt DEAL.

Conflict of Interest

The authors declare no conflict of interest.

Data Availability Statement

The data that support the findings of this study are available from the corresponding author upon reasonable request.

Keywords

ionic conductivity, purity, sodium, solid electrolyte, thiophosphate, tungsten, XPS

Received: June 4, 2025
Revised: July 31, 2025
Published online: September 1, 2025

[1] J. Janek, W. G. Zeier, *Nat. Energy* **2016**, *1*, 16141.
[2] J. Janek, W. G. Zeier, *Nat. Energy* **2023**, *8*, 230.
[3] A. Bielefeld, D. A. Weber, J. Janek, *ACS Appl. Mater. Interfaces* **2020**, *12*, 12821.
[4] L. Zhou, A. Assoud, Q. Zhang, X. Wu, L. F. Nazar, *J. Am. Chem. Soc.* **2019**, *141*, 19002.
[5] M. A. Kraft, S. Ohno, T. Zinkevich, R. Koerver, S. P. Culver, T. Fuchs, A. Senyshyn, S. Indris, B. J. Morgan, W. G. Zeier, *J. Am. Chem. Soc.* **2018**, *140*, 16330.
[6] N. Kamaya, K. Homma, Y. Yamakawa, M. Hirayama, R. Kanno, M. Yonemura, T. Kamiyama, Y. Kato, S. Hama, K. Kawamoto, A. Mitsui, *Nat. Mater.* **2011**, *10*, 682.
[7] Y. Li, S. Song, H. Kim, K. Nomoto, H. Kim, X. Sun, S. Hori, K. Suzuki, N. Matsui, M. Hirayama, T. Mizoguchi, T. Saito, T. Kamiyama, R. Kanno, *Science* **2023**, *381*, 50.
[8] J. Wu, J. Li, X. Yao, *Adv. Funct. Mater.* **2025**, *35*, 2416671.
[9] Y. Tanaka, K. Ueno, K. Mizuno, K. Takeuchi, T. Asano, A. Sakai, *Angew. Chem., Int. Ed.* **2023**, *62*, 202217581.
[10] Z. Wei, L. F. Nazar, J. Janek, *Batter. Supercaps* **2024**, *7*, 202400005.
[11] Z. Zhang, E. Ramos, F. Lalère, A. Assoud, K. Kaup, P. Hartman, L. F. Nazar, *Energy Environ. Sci.* **2018**, *11*, 87.
[12] M. Duchardt, U. Ruschewitz, S. Adams, S. Dehnen, B. Roling, *Angew. Chem., Int. Ed.* **2018**, *57*, 1351.
[13] H. Nguyen, A. Banerjee, X. Wang, D. Tan, E. A. Wu, J.-M. Doux, R. Stephens, G. Verbist, Y. S. Meng, *J. Power Sources* **2019**, *435*, 126623.
[14] A. Hayashi, K. Noi, A. Sakuda, M. Tatsumisago, *Nat. Commun.* **2012**, *3*, 856.
[15] A. Banerjee, K. H. Park, J. W. Heo, Y. J. Nam, C. K. Moon, S. M. Oh, S.-T. Hong, Y. S. Jung, *Angew. Chem.* **2016**, *128*, 9786.
[16] X. Feng, P.-H. Chien, Z. Zhu, I.-H. Chu, P. Wang, M. Immediato-Scuotto, H. Arabzadeh, S. P. Ong, Y.-Y. Hu, *Adv. Funct. Mater.* **2019**, *29*, 1807951.
[17] T. Fuchs, S. P. Culver, P. Till, W. G. Zeier, *ACS Energy Lett.* **2020**, *5*, 146.
[18] I.-H. Chu, C. S. Kompella, H. Nguyen, Z. Zhu, S. Hy, Z. Deng, Y. S. Meng, S. P. Ong, *Sci. Rep.* **2016**, *6*, 33733.
[19] P. Till, M. T. Agne, M. A. Kraft, M. Courty, T. Famprikis, M. Ghidiu, T. Krauskopf, C. Masquelier, W. G. Zeier, *Chem. Mater.* **2022**, *34*, 2410.
[20] C. K. Moon, H.-J. Lee, K. H. Park, H. Kwak, J. W. Heo, K. Choi, H. Yang, M.-S. Kim, S.-T. Hong, J. H. Lee, Y. S. Jung, *ACS Energy Lett.* **2018**, *3*, 2504.
[21] A. Hayashi, N. Masuzawa, S. Yubuchi, F. Tsuji, C. Hotehama, A. Sakuda, M. Tatsumisago, *Nat. Commun.* **2019**, *10*, 5266.
[22] X. Feng, H. Fang, P. Liu, N. Wu, E. C. Self, L. Yin, P. Wang, X. Li, P. Jena, J. Nanda, D. Mitlin, *Angew. Chem., Int. Ed.* **2021**, *60*, 26158.
[23] O. Maus, M. T. Agne, T. Fuchs, P. S. Till, B. Wankmiller, J. M. Gerdes, R. Sharma, M. Heere, N. Jalarvo, O. Yaffe, M. R. Hansen, W. G. Zeier, *J. Am. Chem. Soc.* **2023**, *145*, 7147.

[24] T. Krauskopf, S. P. Culver, W. G. Zeier, *Inorg. Chem.* **2018**, *57*, 4739.
[25] A. Hayashi, K. Noi, N. Tanibata, M. Nagao, M. Tatsumisago, *J. Power Sources* **2014**, *258*, 420.
[26] Y. Yan, Y. Guo, H. Zheng, L. Qi, Y. Yang, Y. Miao, X. Shi, L. Zhang, C. Li, D. Song, *J. Power Sources* **2024**, *620*, 235264.
[27] W. H. Smith, J. Birnbaum, C. A. Wolden, *J. Sulfur Chem.* **2021**, *42*, 426.
[28] E. Zintl, A. Harder, B. G. D. O. Dauth, S. U. T. D. L. Sulfide, N. U. Kaliums, *Z. Für Elektrochem. Angew. Phys. Chem.* **1934**, *40*, 588.
[29] W. H. Zachariasen, H. E. Buckley, *Phys. Rev.* **1931**, *37*, 1295.
[30] H. E. Benito, R. G. Alamilla, J. M. H. Enríquez, F. P. Delgado, D. L. Gutiérrez, P. García, *Adv. Mater. Sci. Eng.* **2015**, *2015*, 325463.
[31] F. El-Kabbany, Y. Badr, M. Tosson, *Phys. Status Solidi A* **1981**, *63*, 699.
[32] S. Bhagavantam, T. Venkatarayudu, *Proc. Indian Acad. Sci.-Sect. A* **1939**, *9*, 224.
[33] R. Steudel, A. Prenzel, *Z. Für Naturforschung B* **1989**, *44*, 1499.
[34] G. J. Janz, J. R. Downey, E. Roduner, G. J. Wasilczyk, J. W. Coutts, A. Eluard, *Inorg. Chem.* **1976**, *15*, 1759.
[35] B.-K. Choi, D. J. Lockwood, *Solid State Commun.* **1989**, *72*, 133.
[36] N. Prieto-Taboada, S. Fdez-Ortiz de Vallejuelo, M. Veneranda, E. Lama, K. Castro, G. Arana, A. Larrañaga, J. M. Madariaga, *J. Raman Spectrosc.* **2019**, *50*, 175.
[37] J. T. Kloprogge, R. L. Frost, *J. Mater. Sci.* **1999**, *34*, 4199.
[38] L. Peter, B. Meyer, *Inorg. Chem.* **1985**, *24*, 3071.
[39] L. Li, Z. Li, R. Zhong, Z. Du, Z. Luan, S. Xi, X. Zhang, *Geophys. Res. Lett.* **2023**, *50*, 2023GL103195.
[40] S. S. Berbano, I. Seo, C. M. Bischoff, K. E. Schuller, S. W. Martin, *J. Non-Cryst. Solids* **2012**, *358*, 93.
[41] O. El Jaroudi, E. Picquenard, N. Gobeltz, A. Demortier, J. Corset, *Inorg. Chem.* **1999**, *38*, 2917.
[42] Y.-C. Lin, Y.-Y. Chen, B.-Y. Yu, W.-C. Lin, C.-H. Kuo, J.-J. Shyue, *Analyst* **2009**, *134*, 945.
[43] M. Fantauzzi, B. Elsener, D. Atzei, A. Rigoldi, A. Rossi, *RSC Adv.* **2015**, *5*, 75953.
[44] M. Pompetzki, M. Jansen, *Z. Für Anorg. Allg. Chem.* **2003**, *629*, 1929.
[45] T. Krauskopf, S. Muy, S. P. Culver, S. Ohno, O. Delaire, Y. Shao-Horn, W. G. Zeier, *J. Am. Chem. Soc.* **2018**, *140*, 14464.
[46] U. Pätzmann, W. Brockner, *Phys. Phys. Chem.* **1983**, *38*, 27.
[47] F. Tsuji, A. Nasu, A. Sakuda, M. Tatsumisago, A. Hayashi, *J. Power Sources* **2021**, *506*, 230100.
[48] T. Famprikis, H. Bouyanfif, P. Canepa, M. Zbiri, J. A. Dawson, E. Suard, F. Fauth, H. Y. Playford, D. Dambournet, O. J. Borkiewicz, M. Courty, O. Clemens, J.-N. Chotard, M. S. Islam, C. Masquelier, *Chem. Mater.* **2021**, *33*, 5652.
[49] X. Chi, Y. Zhang, F. Hao, S. Kmiec, H. Dong, R. Xu, K. Zhao, Q. Ai, T. Terlier, L. Wang, L. Zhao, L. Guo, J. Lou, H. L. Xin, S. W. Martin, Y. Yao, *Nat. Commun.* **2022**, *13*, 2854.
[50] S. Kmiec, K. Krupp, E. Ruoff, A. Manthiram, *Chem. Mater.* **2024**, *36*, 7867.
[51] R. Gresch, W. Müller-Warmuth, H. Dutz, *J. Non-Cryst. Solids* **1979**, *34*, 127.
[52] M. Shimoda, M. Maegawa, S. Yoshida, H. Akamatsu, K. Hayashi, P. Gorai, S. Ohno, *Chem. Mater.* **2022**, *34*, 5634.
[53] H. Nakajima, H. Tsukasaki, J. Ding, T. Kimura, T. Nakano, A. Nasu, A. Hirata, A. Sakuda, A. Hayashi, S. Mori, *J. Power Sources* **2021**, *511*, 230444.
[54] M. Pompetzki, R. E. Dinnebier, M. Jansen, *Solid State Sci.* **2003**, *5*, 1439.
[55] A. Müller, E. Diemann, R. Jostes, H. Bögge, *Angew. Chem. Int. Ed. Engl.* **1981**, *20*, 934.
[56] A. Berkdemir, H. R. Gutiérrez, A. R. Botello-Méndez, N. Perea-López, A. L. Elías, C.-I. Chia, B. Wang, V. H. Crespi, F. López-Urías, J.-C. Charlier, H. Terrones, M. Terrones, *Sci. Rep.* **2013**, *3*, 1755.
[57] Z. Zhang, Y. Qiu, W. Yan, Z. Zhou, Y. Yao, X. Liu, J. Sun, Y. Li, *Nanoscale Adv.* **2022**, *4*, 1626.
[58] W. Weng, G. Liu, Y. Li, L. Shen, X. Yao, *Appl. Mater. Today* **2022**, *27*, 101448.
[59] M. Lazar, S. Kmiec, A. Joyce, S. W. Martin, *ACS Appl. Energy Mater.* **2020**, *3*, 11559.
[60] T. Takayanagi, A. Nasu, F. Tsuji, K. Motohashi, A. Sakuda, M. Tatsumisago, A. Hayashi, *J. Ceram. Soc. Jpn.* **2022**, *130*, 498.
[61] S. Wenzel, T. Leichtweiss, A. W. Weber, J. Sann, W. G. Zeier, J. Janek, *ACS Appl. Mater. Interfaces* **2016**, *8*, 28216.
[62] M. Jansen, U. Henseler, *J. Solid State Chem.* **1992**, *99*, 110.
[63] P. Juhás, T. Davis, C. L. F. Farrow, S. J. L. Billinge, *J. Appl. Crystallogr.* **2013**, *46*, 560.
[64] C. L. Farrow, P. Juhas, J. W. Liu, D. Bryndin, E. S. Božin, J. Bloch, T. Proffen, S. J. L. Billinge, *J. Phys. Condens. Mat.* **2007**, *19*, 335219.